

Chapter 7

The Iron Project: Photoionization and Photoexcitation of Fe XVII in Solar Opacity

Sultana N. Nahar

Abstract Opacity is a fundamental quantity for plasmas and gives a measure of radiation transport. It is caused by the absorption and emission of photons by the constituent elements of the plasma and hence depends mainly on the atomic processes of photoexcitation and photoionization. It is also affected by photon scatterings. Monochromatic opacity at a particular frequency, $\kappa(\nu)$, is obtained from oscillator strengths (f) for bound-bound transitions and photoionization cross sections (σ_{PI}). However, the total monochromatic opacity depends on the summed contributions of all possible transitions from all ionization stages of all elements in the plasma. Calculation of accurate atomic parameters for such a large number of transitions has been the main problem for obtaining accurate opacities. The overall mean opacity, such as Rosseland mean opacity (κ_R), depends also on the physical conditions, such as temperature and density, elemental abundances and equation-of-state such as local thermodynamic equilibrium (LTE) of the plasmas.

In this report, I will illustrate the necessity for high-precision atomic calculations for the radiative processes of photoexcitation and photoionization in order to resolve some perplexing astrophysical problems, particularly solar abundances and opacities. Fe XVII is most abundant iron ion in the solar convection zone. I will present new results on oscillator strengths and new features in high energy photoionization cross sections of Fe XVII which give clear indication of the reason for discrepancy between measured and theoretically predicted abundances and on how the discrepancy is resolved or reduced.

7.1 Introduction

The fundamental quantity opacity (κ) is needed for studying various quantities such as elemental abundances, diffusion of radiation, optical depth, speed of seismic waves, stellar pulsations etc. of astrophysical and laboratory plasmas. As the radiation propagates, it loses energy as well as slows down by absorption and emission

S.N. Nahar (✉)

Department of Astronomy, The Ohio State University, Columbus, OH 43210, USA
e-mail: nahar@astronomy.ohio-state.edu

by the constituent elements. The resultant effect is the opacity such that more radiation means less opacity and vice versa. Because of opacity the high energy gamma radiation produced by the nuclear fusion in the core of the sun takes over a million years to travel to the surface and escape as optical or low energy photons. Opacity depends on the atomic process of photoexcitations, photoionization and photon scattering.

For the photon-ion interactions, calculations of opacity depends on the oscillator strengths and photoionization cross sections. Consideration of these processes require large amount of atomic data for all possible radiative transitions. Currently available atomic data for all ions are not accurate and complete enough to compute accurate opacities for various astrophysical problems.

7.1.1 The Opacity Project and the Iron Project

Prior to the Opacity Project (OP) [26, 28, 29], there were large discrepancies between astrophysical observations and theoretical predictions obtained using existing opacities for plasmas. The earlier opacities using the atomic data from simple approximations were incorrect by factors of 2 to 5 resulting in inaccurate stellar models. The international collaborative effort, the Opacity Project, of about 25 scientists from 6 countries was initiated in 1982 in order to study in detail and obtain accurate atomic data of radiative processes with large number of states and apply them for computation of accurate opacities. The first systematic and detailed studies were carried out for the radiative processes of photoexcitation and photoionization for all astrophysically abundant atoms and ions from hydrogen to iron. Computations were carried out in ab initio close coupling approximation and using R -matrix method. Large amount of atomic data for energy levels, oscillator strengths and photoionization cross sections were obtained and are made available at data base TOPbase [31] at CDS. The monochromatic opacities and Rosseland mean opacities under the OP are available at the OPserver [22] at the Ohio Supercomputer Center (OSC). New features in photoionization cross sections were revealed. Many long standing astrophysical problems were solved. These atomic data have continued to solve many astrophysical problems. However, a large part of the data are not precise and complete enough for various diagnostics and astrophysical problems.

Following the successful collaboration of the OP, the international collaboration of the Iron Project (IP) [6] was initiated to focus on collisional processes as well as radiative processes, but mainly for the astrophysically abundant iron and iron-peak elements. Work under IP emphasizes the relativistic effects and achievement of higher accuracy. The large amount of atomic data from the IP are available at TIPbase [30] at CDS, at *Atomic Data and Nuclear Data Tables* database and at the NORAD-Atomic-Data website [21]. A new project, RMAX, was also initiated under the IP to focus on the X-ray astrophysics.

The OP team made extensive extension of the existing R -matrix codes for the radiative processes [2]. The computations under the OP were carried out in non-relativistic LS coupling approach. The OP R -matrix IP were extended to include

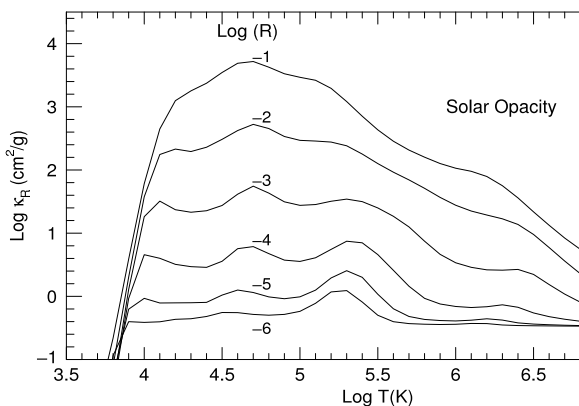


Fig. 7.1 Opacities in temperature-density regimes throughout the solar interior. κ is the Rosseland mean opacity and $R = \rho(g/cc)/T_6^3$ is the temperature-density parameter with $T_6 = 10^6$ K, i.e. $T_6 = T * 10^{-6}$. For the sun, $-6 \leq R \leq -1$. The four bumps in the curves of various R represent H-, He-, Z-, and inner-shell bumps, that is, higher opacities due to excitation/ionization of the atomic species at those temperatures [27]

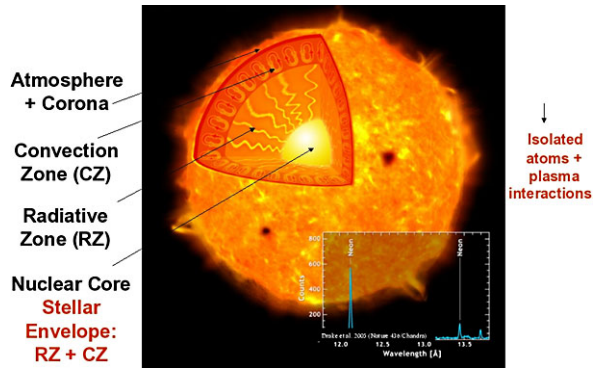
relativistic fine structure effects in Breit-Pauli approximation under the IP and the new method of computation is known as the Breit-Pauli R -matrix or BPRM method [3]. Several extension and modifications of the codes were made by the Ohio state team of the IP (e.g. [4, 19]).

Considerable advances in computational capabilities for higher accuracy is continuing. Higher order relativistic corrections have been added to the BPRM method [4]. Theoretical spectroscopy has been developed for identification of large number of fine structure levels for all practical purposes [10, 15]. This enables calculation of accurate oscillator strengths for larger number of transitions than considered before. We are also finding existence of extensive and dominant resonant features in the high energy photoionization cross sections (e.g. [13]) as well as important fine structure effects in low energy region [19]. We will illustrate results from recent calculations showing more complete atomic data and new features and considerable improvement in accuracy in monochromatic opacities, particularly Fe XVII opacity in the sun.

7.2 High Temperature Plasmas in Solar Corona and Abundances

The solar elemental abundances are known within 10 % uncertainty as: H—90 % (by number) and 70% (by mass fraction), He—10 % (by number) and 28 % (by mass), and metals (all elements heavier than helium)—2 % (by mass) (e.g. [23]). Using the OP data and standard mixture of solar elemental abundances, solar opacity were calculated under the OP as shown in Fig. 7.1 [27]. The curves of various R in the figure show about four bumps or kinks, representing higher opacities. These are

Fig. 7.2 Solar interior is defined from the core to the end of the convection zone. At the convection zone plasma bubbles and the radiation escapes



due to excitation/ionization, and hence higher absorption of photons, of different atomic species at those temperatures. The first bump is the H-bump, the second one is the He-bump, the third one the Z-bump (sum of all elements heavier than H and He) and the fourth one is due to inner-shell excitation/ionization bump. The general features of these solar opacity curves are in agreement with those by the other opacity by OPAL [7, 8].

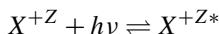
However, these do not solve require precision for elemental abundances for various applications. For example, the recent determination of solar abundances of light elements, from measurements and 3D hydro NLTE models, show 30–40 % lower abundances of C, N, O, Ne, Ar than the standard abundances; these contradict the accurate helioseismology data. One major problem has been the discrepancy between the observed and predicted boundary between the solar radiative zone and the convection zone, R_{CZ} . Radiation from the solar nuclear core travels through the radiative zone to the convection zone where the phase changes as the plasma bubbles and beyond it the photons escape. From helioseismology, the distance of boundary R_{CZ} , relative to the solar radius, is accurately measured to be 0.713 (Fig. 7.2). R_{CZ} can be calculated from opacity through optical depth and elemental abundances in the solar plasma. However, the calculated boundary R_{CZ} is 0.726, is a much larger value than the measured value. The plasma in the convection zone is in a HED (high energy density) condition where the temperature is $T_e \sim 193$ eV (about 2.2 MK) and the electron density is $n_e \sim 10^{23}/\text{cm}^3$. At this condition, the abundant elements are O, Ne, especially Fe ions in the ionic states of Fe XVII, Fe XVIII, and Fe XIX, Fe XVII the most.

The plasma in the solar convection zone has been under study to resolve the discrepancy. With technological advances, the laboratory set-up zeta pinch or Z-pinch machines, which can confine plasma through intense magnetic field, at the Sandia National Lab (SNL) is now able to create this plasma condition and study the radiation transmission, the inverse of opacity. The measurements will enable calibration of the theoretical calculations of basic parameters that govern the opacity. Bailey et al. [1] reported achieving HED plasmas at temperature ($T > 10^6$ K) and density ($N > 10^{20} \text{ cm}^{-3}$) similar to those in the convection zone. At the Z-pinch set-up the plasma is created with laser heating and compress or implode the plasma by a gigantic magnetic field created by about 27 MAmp current passing through the coil

around it. The measurement at SNL Z-pinch machine showed that the measured iron opacity is much higher than the prediction obtained using the radiative atomic data, oscillator strengths for photoexcitation and cross sections for photoionization, from the Opacity Project.

7.3 Photoexcitation, Photoionization and Opacity

Opacity $\kappa(\nu)$ depends on oscillator strengths of photoexcitation,

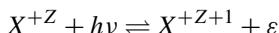


where X^{+Z} is the ion with charge Z and the inverse arrow represents de-excitation. The emitted or absorbed photon ($h\nu$) from the transition is observed as a spectral line. The relevant atomic parameters for the direct and inverse processes are oscillator strength (f) and radiative decay rate (A -value). f_{ij} is related to $\kappa(\nu)$ as

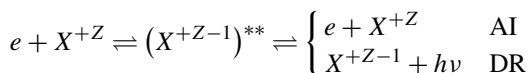
$$\kappa_\nu(i \rightarrow j) = \frac{\pi e^2}{mc} N_i f_{ij} \phi_\nu \quad (7.1)$$

where N_i is the ion density in state i , ϕ_ν is a profile factor which can be Gaussian, Lorentzian, or combination of both over a small wavelength range.

Photoionization can be direct when an electron is ejected with absorption of a photon,



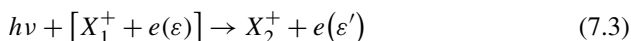
where the inverse process is radiative recombination (RR). Photoionization also occurs via an intermediate doubly excited autoionizing state:



A colliding electron excites the target and attaches to form the short-lived doubly excited autoionizing state which leads either to autoionization (AI), where the electron goes free and target drops to ground state, or to dielectronic recombination (DR), where the electron gets bound by emission of a photon. The inverse of DR is photoionization. The autoionizing state manifests as an enhancement or resonance in the process and can be seen in absorption spectra. The atomic parameters for these processes are photoionization cross sections (σ_{PI}) and recombination rates. $\kappa(\nu)$ for photoionization is obtained from σ_{PI} as

$$\kappa_\nu = N_i \sigma_{\text{PI}}(\nu) \quad (7.2)$$

κ_ν also has contributions from two other processes, inverse bremsstrahlung or free-free (ff) scattering and photon-electron scattering. Bremsstrahlung refers to the radiation emitted by a charged particle accelerated in an electromagnetic field. The inverse process is where a free electron and an ion can absorb a photon in free-free interaction, that is,



Explicit calculations for the free-free scattering cross sections may be done using the elastic scattering matrix elements for electron impact excitation of ions. An approximate expression for the free-free opacity is given by

$$\kappa_{\nu}^{\text{ff}}(1, 2) = 3.7 \times 10^8 N_e N_i g_{\text{ff}} \frac{Z^2}{T^{1/2} \nu^3} \quad (7.4)$$

where g_{ff} is a Gaunt factor.

The photon-electron scattering, giving some contributions to opacity, can be of two type, Thomson scattering, when the electron is free and Rayleigh scattering when the electron is bound to an atomic or molecular species. κ is related to Thomson scattering cross section σ^{Th} as,

$$\kappa(sc) = N_e \sigma^{\text{Th}} = N_e \frac{8\pi e^4}{3m^2 c^4} = 6.65 \times 10^{-25} \text{ cm}^2/\text{g} \quad (7.5)$$

To Rayleigh scattering cross section σ^R , opacity is related as

$$\kappa_{\nu}^R = n_i \sigma_{\nu}^R \approx n_i f_i \sigma^{\text{Th}} \left(\frac{\nu}{\nu_I} \right)^4 \quad (7.6)$$

where n_i is the density of the atomic or molecular species, $h\nu_I$ is the binding energy and f_i is the total oscillator strength associated with the bound electron, i.e. the sum of all possible transitions, such as the Lyman series of transitions $1s \rightarrow np$ in hydrogen.

To find the average opacity, such as Rosseland opacity κ_R , we need elemental abundances pertinent to the plasma conditions of temperature and density. These are obtained from proper equation-of-state (EOS) which gives the ionization fractions and level populations of each ion of an element in levels with non-negligible occupation probability. For example, for plasmas in local thermodynamic equilibrium (LTE) Saha equation is the EOS. However, Saha equation is not applicable in non-LTE condition. Some details of the opacity calculations can be found in [23].

Rosseland mean opacity $\kappa_R(T, \rho)$ is the harmonic mean of monochromatic opacity averaged over the Planck function, $g(u)$,

$$\frac{1}{\kappa_R} = \frac{\int_0^{\infty} \frac{1}{\kappa_{\nu}} g(u) du}{\int_0^{\infty} g(u) du}, \quad (7.7)$$

where $g(u)$ is given by

$$g(u) = \frac{15}{4\pi^4} \frac{u^4 e^{-u}}{(1 - e^{-u})^2}, \quad u = \frac{h\nu}{kT} \quad (7.8)$$

$g(u)$, for an astrophysical state is calculated with different chemical compositions H (X), He (Y) and metals (Z), such that

$$X + Y + Z = 1 \quad (7.9)$$

7.4 Theoretical Approach: Breit-Pauli R -Matrix Method

As mentioned above, the relativistic Breit-Pauli R -matrix method with close coupling (CC) approximation is used to calculate the oscillator strengths and photoionization cross sections. (Details are given in [23]). The BPRM Hamiltonian is given by

$$H^{\text{BP}} = H^{\text{NR}} + H^{\text{mass}} + H^{\text{Dar}} + H^{\text{so}} \quad (7.10)$$

$$+ \frac{1}{2} \sum_{i \neq j}^N [g_{ij}(so + so') + g_{ij}(ss') + g_{ij}(css') + g_{ij}(d) + g_{ij}(oo')] \quad (7.11)$$

where H^{NR} is the nonrelativistic Hamiltonian,

$$H^{\text{NR}} = \sum_{i=1}^N \left\{ -\nabla_i^2 - \frac{2Z}{r_i} + \sum_{j>i}^N \frac{2}{r_{ij}} \right\} \quad (7.12)$$

and the one-body relativistic correction terms are mass correction, Darwin and spin-orbit interaction terms respectively,

$$H^{\text{mass}} = -\frac{\alpha^2}{4} \sum_i p_i^4, \quad H^{\text{Dar}} = \frac{\alpha^2}{4} \sum_i \nabla^2 \left(\frac{Z}{r_i} \right), \quad H^{\text{so}} = \left[\frac{Ze^2 \hbar^2}{2m^2 c^2 r^3} \right] \quad (7.13)$$

The spin-orbit interaction H^{so} splits LS energy in to fine structure levels. Rest of the terms are two-body interaction terms where the notation are s for spin and a prime indicates ‘other’, o for orbit, c for contraction, and d for Darwin. These terms are much weaker but can become important for weak transitions and when relativistic effects are important. The first two two-body terms comprise the Breit interaction

$$H^{\text{B}} = \sum_{i>j} [g_{ij}(so + so') + g_{ij}(ss')] \quad (7.14)$$

which contributes more relatively to the other terms. In the latest development of the BPRM codes, Breit interaction has been included [4].

In CC approximation, the wave function expansion is expressed as a core or target ion of N -electrons interacting with the $(N + 1)$ interacting electron. The total wave function expansion is expressed as:

$$\Psi_E(e + \text{ion}) = A \sum_i^N \chi_i(\text{ion}) \theta_i + \sum_j c_j \Phi_j(e + \text{ion}) \quad (7.15)$$

where χ_i is the target ion or core wave function which includes excitations. θ_i is interacting electron wave function (continuum or bound), and Φ_j is a correlation function of $(e + \text{ion})$. The complex resonant structures in the atomic processes are included through coupling of bound and continuum channels with core excitations.

The target wave functions χ_i are obtained from atomic structure calculations, e.g. SUPERSTRUCTURE (SS) [5, 18].

Substitution of $\Psi_E(e + \text{ion})$ in $H\Psi_E = E\Psi_E$ results in a set of coupled equations which are solved by the R -matrix method. In the R -matrix method (Fig. 7.5), the space is divided in two regions, the inner and the outer regions, of a sphere of radius r_a with the ion at the center. r_a , the R -matrix boundary, is chosen large enough for electron-electron interaction potential to be zero outside the boundary. The wave function at $r > r_a$ is Coulombic due to perturbation from the long-range multipole potentials. In the inner region, the partial wave function of the interacting electron is expanded in terms of a basis set, called the R -matrix basis, and are made continuous at the boundary by matching with the Coulomb functions outside the boundary. For negative energy, the solution is a bound ($e + \text{ion}$) states, Ψ_B and for positive energy, the solution is a continuum state, Ψ_F .

The oscillator strengths and photoionization cross sections are obtained from the line strength \mathbf{S} . It depends on the transitions matrix elements with dipole operator $\mathbf{D} = \sum_i \mathbf{r}_i$ for photoexcitation and photoionization:

$$\langle \Psi_B \| \mathbf{D} \| \Psi_{B'} \rangle, \quad \langle \Psi_B \| \mathbf{D} \| \Psi_F \rangle \quad (7.16)$$

respectively. The reduced tensor $\|\mathbf{D}\|$ gives 3- j symbols for angular momenta on simplification and the generalized line strength as

$$S = \left\langle \left| \Psi_f \sum_{j=1}^{N+1} r_j \Psi_i \right| \right\rangle^2 \quad (7.17)$$

The oscillator strength (f_{ij}) and radiative decay rate (A_{ji}) for the bound-bound transition are obtained as

$$f_{ij} = \left[\frac{E_{ji}}{3g_i} \right] S, \quad A_{ji} (\text{sec}^{-1}) = \left[0.8032 \times 10^{10} \frac{E_{ji}^3}{3g_j} \right] S \quad (7.18)$$

The photoionization cross section, σ_{PI} , is obtained as

$$\sigma_{\text{PI}} = \left[\frac{4\pi}{3c} \frac{1}{g_i} \right] \omega S, \quad (7.19)$$

where ω is the incident photon energy in Rydberg unit. With consideration of relativistic fine structure effects, BPRM method enables extensive sets of E1 transitions ($\Delta j = 0, \pm 1, \Delta L = 0, \pm 1, \pm 2$, parity π changes) with same spin-multiplicity ($\Delta S = 0$) and intercombination ($\Delta S \neq 0$). On the contrary LS coupling allows only same spin-multiplicity transitions.

Under the IP, large sets of various forbidden transitions are also considered. They are obtained in Breit-Pauli approximation but using atomic structure calculations. Due to small f -values, typically the radiative decay rates, A -values, are calculated for the forbidden transitions. These transitions are mainly

- (i) electric quadrupole (E2) transitions ($\Delta J = 0, \pm 1, \pm 2$, parity does not change)

$$A_{ji}^{\text{E2}} = 2.6733 \times 10^3 \frac{E_{ij}^5}{g_j} S^{\text{E2}}(i, j) \text{ s}^{-1}, \quad (7.20)$$

(ii) magnetic dipole (M1) transitions ($\Delta J = 0, \pm 1$, parity does not change),

$$A_{ji}^{M1} = 3.5644 \times 10^4 \frac{E_{ij}^3}{g_j} S^{M1}(i, j) \text{ s}^{-1}, \quad (7.21)$$

(iii) electric octupole (E3) transitions ($\Delta J = \pm 2, \pm 3$, parity changes) and

$$A_{ji}^{E3} = 1.2050 \times 10^{-3} \frac{E_{ij}^7}{g_j} S^{E3}(i, j) \text{ s}^{-1}, \quad (7.22)$$

(iv) magnetic quadrupole (M2) transitions ($\Delta J = \pm 2$, parity changes) and

$$A_{ji}^{M2} = 2.3727 \times 10^{-2} \text{ s}^{-1} \frac{E_{ij}^5}{g_j} S^{M2}(i, j). \quad (7.23)$$

Some details of the forbidden transitions are given in [11, 18].

7.5 Results and Discussions

The accuracy and completeness of oscillator strengths for bound-bound transitions and new features in photoionization affecting the plasma opacities are discussed with examples in the two subsections below. Results on opacity is discussed in the third subsection.

7.5.1 Energy Levels and Oscillator Strengths

In order to obtain accurate solar opacity at the convection zone, we have been focusing on the radiative data for the most abundant iron ions, Fe XVII–Fe XIX. The oscillator strengths of these ions have already been obtained [12, 14, 18]. We have completed the photoionization data for Fe XVII recently [20]. Being complex with strong electron-electron correlation, computation of radiative data for each iron ion is a challenge. Another major task is the spectroscopic identification of the large number of energy levels and transitions that BPRM method can compute. BPRM identification is quite different from atomic structure calculations where identification of an energy level is based on the percentage contributions of the configurations. The BPRM Identification is carried out using a method based on the channel contributions in the outer region of the R -matrix method, quantum defect theory, and algebraic algorithms [10, 15].

BPRM calculations for Fe XVII transitions under the IP resulted in a total of 490 fine structure energy levels of total angular momenta $0 \leq J \leq 7$ of even and odd parities with $2 \leq n \leq 10$, $0 \leq l \leq 8$, $0 \leq L \leq 8$, and singlet and triplet multiplicities. These energies agree within 1 % with all available 52 measured energies. The calculated levels yielded to over 2.6×10^4 allowed (E1) transitions that are of dipole and intercombination type. In addition a set of 2312 forbidden transitions of

Table 7.1 Example set of dipole allowed and intercombination transitions in Fe XVII. The $g : I$ indices refer to the statistical weight:energy level index. The notation $a(b)$ means $a \times 10^b$

C_i	C_j	T_i	T_j	$g_i : I_i$	$g_j : I_j$	$\lambda_{ij}/\text{\AA}$	f	$A \cdot s$
2p6	2s22p53s	$^1S^e$	$^3P^o$	1 : 1	3 : 1	17.1	1.223(-1)	9.35(11)
2p6	2s22p63s	$^1S^e$	$^1P^o$	1 : 1	3 : 2	16.8	1.008(-1)	7.96(11)
2p6	2s22p53d	$^1S^e$	$^3P^o$	1 : 1	3 : 3	15.4	8.136(-3)	7.58(10)
2p6	2s22p53d	$^1S^e$	$^3D^o$	1 : 1	3 : 4	15.3	6.208(-1)	5.93(12)
2p6	2s22p53d	$^1S^e$	$^1P^o$	1 : 1	3 : 5	15.0	2.314	2.28(13)
2p6	2s2p63p	$^1S^e$	$^3P^o$	1 : 1	3 : 6	13.9	3.501(-2)	4.03(11)
2p6	2s2p63p	$^1S^e$	$^1P^o$	1 : 1	3 : 7	13.8	2.835(-1)	3.30(12)
2p6	2s22p54s	$^1S^e$	$^3P^o$	1 : 1	3 : 8	12.7	2.286(-2)	3.16(11)
2p6	2s22p54s	$^1S^e$	$^1P^o$	1 : 1	3 : 9	12.5	1.758(-2)	2.49(11)
2p6	2s22p54d	$^1S^e$	$^3P^o$	1 : 1	3 : 10	12.3	3.281(-3)	4.81(10)
2p6	2s22p54d	$^1S^e$	$^3D^o$	1 : 1	3 : 11	12.3	3.594(-1)	5.31(12)
2p53s	2s22p53p	$^3P^o$	$^3P^e$	3 : 1	1 : 2	296.0	3.354(-2)	7.66(09)
2p53s	2s22p53p	$^3P^o$	$^3P^e$	3 : 1	3 : 4	262.7	5.893(-5)	5.70(06)
2p53s	2s22p53p	$^3P^o$	$^3P^e$	5 : 1	3 : 4	252.5	4.985(-3)	8.69(08)
2p53s	2s22p53p	$^3P^o$	$^3P^e$	3 : 1	5 : 2	340.4	9.075(-2)	3.13(09)
2p53s	2s22p53p	$^3P^o$	$^3P^e$	5 : 1	5 : 2	323.5	6.913(-2)	4.41(09)
LS		$^3P^o$	$^3P^e$	9	9		8.959(-2)	6.71(09)
2p63s	2s22p53p	$^1P^o$	$^3P^e$	3 : 2	1 : 2	413.8	9.557(-3)	1.12(09)
2p63s	2s22p53p	$^1P^o$	$^3P^e$	3 : 2	3 : 4	351.6	4.162(-2)	2.25(09)
2p63s	2s22p53p	$^1P^o$	$^3P^e$	3 : 2	5 : 2	506.3	1.464(-3)	2.29(07)
2p53p	2s22p53d	$^3P^e$	$^3P^o$	1 : 2	3 : 3	369.5	9.560(-3)	1.56(08)
2p53p	2s22p53d	$^3P^e$	$^3P^o$	3 : 4	1 : 2	457.5	1.443(-3)	1.38(08)
2p53p	2s22p53d	$^3P^e$	$^3P^o$	3 : 4	3 : 3	439.0	1.262(-3)	4.37(07)
2p53p	2s22p53d	$^3P^e$	$^3P^o$	3 : 4	5 : 2	415.7	5.280(-4)	1.22(07)
2p53p	2s22p53d	$^3P^e$	$^3P^o$	5 : 2	3 : 3	317.7	9.904(-3)	1.09(09)
2p53p	2s22p53d	$^3P^e$	$^3P^o$	5 : 2	5 : 2	305.4	5.093(-2)	3.64(09)
LS		$^3P^e$	$^3P^o$	9	9		3.145(-2)	1.64(09)

types E2, M1, E3, and M2 were also obtained. These transitions correspond to an order of magnitude more atomic data available data for Fe XVII. Table 7.1 gives an example set of Fe XXVII transitions that have been identified and processed in the standard NIST format.

The effect of accuracy and more complete set of transitions on opacities was tested for Fe IV in a plasma with temperature $\log T(K) = 4.5$ and electron density $\log N_e(\text{cm}^{-3}) = 17.0$, where Fe IV dominates the iron opacity. It was found by Nahar and Pradhan [16] that iron opacity κ_ν for that plasma depends primarily on oscillator strengths, and varies over orders of magnitude between 500–4000 \AA . Sig-

nificant differences and shifts of opacity was found with the opacity obtained using from earlier oscillator strengths calculated under the OP.

7.5.2 High Energy Photoionization

Most of the opacity caused by photoionization is through the photon absorption at resonant energies. The resonances in photoionization are introduced as the core goes through excitations. The OP work computed the resonances in photoionization of the ground and many excited states of many atomic systems for the first time. However, the work considered only the low energy resonances with the assumption that they are more dominant due to strong couplings of channels, and that couplings become weaker with higher energy and photoionization becomes featureless and decays smoothly. However, later investigations under the IP revealed that resonances due to excitations of the high lying core states of ions, such as for Fe XXI, are much stronger and hence play a very important role for opacities [13].

We found extensive dominance of high-peak resonances in the high energy photoionization of Fe XVII in our recent investigations [20, 33]. There is a large energy gap of about 47 Rd between the core states of $n = 2$ and $n = 3$ complexes. Such large gap is often taken as vanished impact of the channels with $n = 3$ core levels with the lower ones. Hence earlier calculations considered only 3 levels of the $n = 2$ complex [24]. It is also known that the $n = 3$ excitations do not form any bound state of Fe XVII. However, large radiative decay rates of $n = 3$ levels indicated possibility of high autoionizing resonances and were found to be the fact in the 60 level calculations as shown in Fig. 7.3.

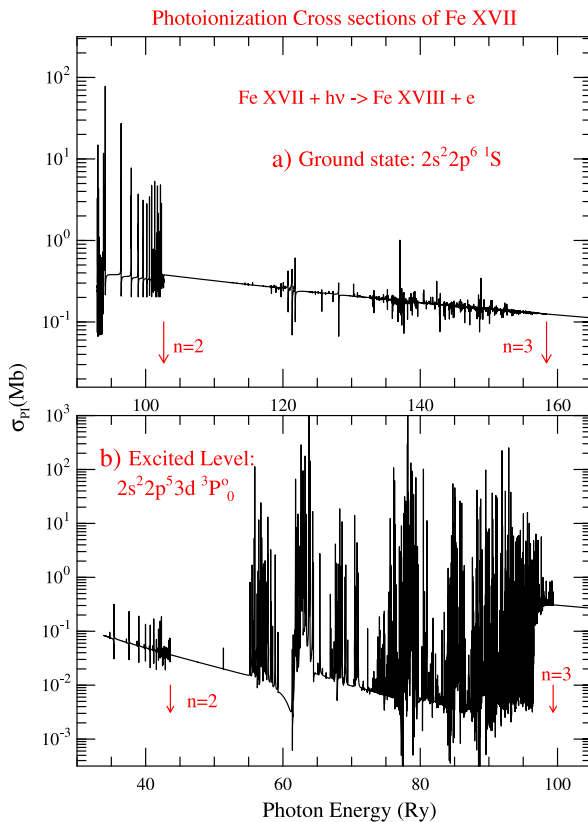
Figure 7.3 presents σ_{PI} of the (a) ground level $2s^22p^6(^1S_0)$ and (b) an excited level $2s^22p^53d(^3P_0^o)$ of Fe XVII. The resonances due to $n = 3$ levels of the core do not have much impact, except appearing as some weak resonances, on the ground level. While resonances introduced by the core excitations to $n = 2$ levels are important for the ground level, excitations to $n = 3$ levels are more important for the excited level photoionization. The high energy region of σ_{PI} of the excited level is filled with high-peak resonances.

Most of these resonances in Fig. 7.3 are Rydberg series autoionizing resonances. They form at energies E_p ,

$$(E_t - E_p) = z^2/\nu^2$$

where E_t is an excited core state or threshold and ν is the effective quantum number of the state. These resonances are usually narrow and more common. However, photoionization of excited levels is characterized by wide PEC (photoexcitation-of-core) or Seaton resonances. These resonances occur when the core goes through a dipole allowed transition while the outer electron remains as a spectator. The state is followed by ionization via the outer electron while the core drops down to the ground state. Since the ground level of core Fe XVIII is $2s^22p^5(^2P_{3/2}^o)$, a PEC resonance can form at the excited energy threshold of the core when it goes through

Fig. 7.3 Photoionization cross section σ_{PI} of Fe XVII with arrows pointing energy limits of $n = 2$ and 3 core states. *Top*: ground level, $n = 2$ resonances are important and for an excited level. *Bottom*: $n = 3$ resonances are important

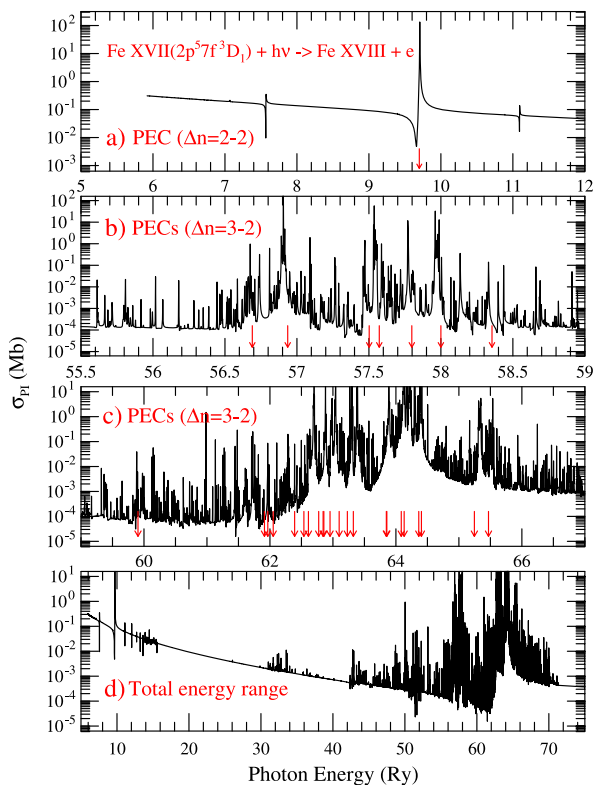


the dipole transition, for example, $2s^2 2p^5 (^2P_{3/2}^o) - 2s^2 2p^4 3s (^2P_{3/2})$. The resonant phenomena was first explained by Seaton in [32].

Figure 7.4 presents σ_{PI} of the excited level, $2s^2 2p^5 7f (^3D_1)$, of Fe XVII. The 60 core levels includes 29 possible dipole allowed transitions for the core ground level and each corresponds to a Seaton resonance. The cross sections are delineated at 24,653 energies; the energy intervals are chosen so as to resolve resonance profiles in so far as practical. The overlapping Seaton resonances have been pointed by couple of arrows in the figure. As the figure shows, Seaton resonances are strong which increase the background cross sections by orders of magnitude. The shape and strength of PEC resonances depend on the interference of core excitations and overlapping Rydberg series of resonances. These dominating features, especially those due to $\Delta n = 3-2$ core transitions, show large enhancement of photon absorptions related to the opacities. These are non-existent in the available data and thereby grossly underestimating the opacity.

The impact of the myriad $\Delta n(3-2)$ PECs in Fig. 7.4b and 7.4c, can be seen to dominate the distribution of oscillator strength over a large region $\sim 56-66$ Ry, or >100 eV, due to the L-shell excitation array $2p \rightarrow 3d$. The cumulative resonance

Fig. 7.4 Photoionization cross section (σ_{PI}) of excited level $2p^37f^3D_1$ over various ranges of energy (a, b, c) while the bottom panel (d) presents the total range. PEC resonances appear, positions pointed by *arrows*, occur at energies of dipole transitions in the core. They are high-peak, wider and enhance the background σ_{PI} by orders of magnitude, and will affect photoionization and recombination rates, especially of high temperature plasmas



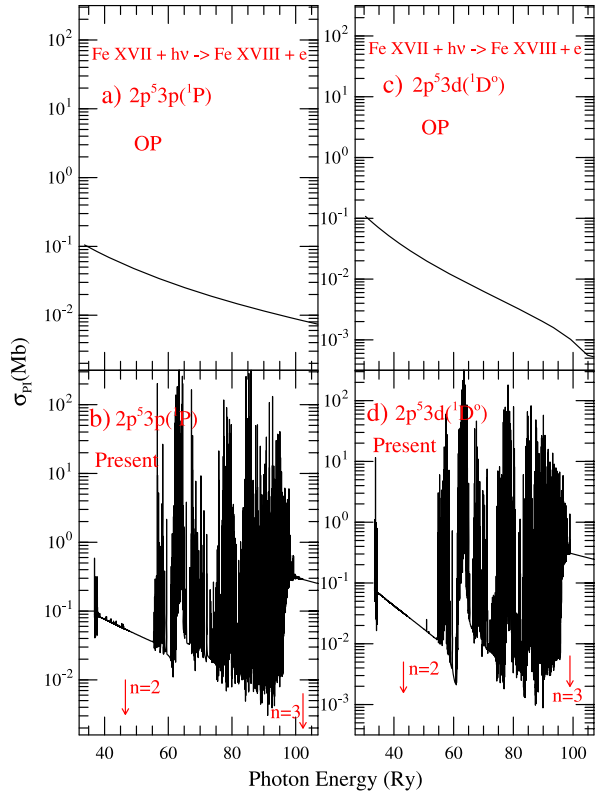
(or bound-free continuum) oscillator strength corresponding to Fig. 7.4 is related to the photoionization cross section (viz. [17]) as

$$f_r [{}^3D_1 \longrightarrow \varepsilon SLJ : {}^3(P, D, F) (J = 0, 1, 2)^o] = \left[\frac{1}{4\pi\alpha a_o^2} \right] \int_0^{\varepsilon_0} \sigma_{PI}(2s^22p^57f^3D_1) d\varepsilon, \quad (7.24)$$

where ε is the energy relative to ionization threshold and up to $\varepsilon_0 \sim 80$ Ry. An integration over the range shown in Fig. 7.4 yields the *partial* resonance oscillator strength including all of the PECs and the non-PEC resonances due to coupling of all 60 Fe XVIII levels. The sum over the oscillator strengths corresponding to the 30 PECs gives a total $f_{PEC} = 2.31$. The integrated resonance oscillator strength f_r is found to be 4.38. Hence, the 30 PEC resonances involving transitions up to the $n = 3$ levels of the core ion Fe XVIII contribute over half of all the continuum bound-free oscillator strength in photoionization of *any* excited state of Fe XVII. Although we chose an excited level to demonstrate the quantitative effect of PEC resonances; they manifest themselves in photoionization of most levels.

σ_{PI} of two levels of Fe XVII obtained from 60CC BPRM calculations and from the OP are compared in Fig. 7.5. Panels (a, b) shows σ_{PI} of level $2p^53p({}^1P)$ and panels (c, d) of level $2p^53d({}^1D^o)$, respectively. Comparison shows low and smooth

Fig. 7.5 Comparison of photoionization cross sections σ_{PI} between 60CC calculations and from the OP (see [31]) for excited singlet levels (no fine structure): (a, b) $2p^53p(^1P)$, and (c, d) $2p^53d(^1D^o)$. The comparisons demonstrate that without inclusion of $n = 3$ core levels of Fe XVIII, σ_{PI} is considerably underestimated throughout most of the high energy region. These resonances are included as *lines* in the OP work [28, 29], as in other opacities calculations [7, 8]



background in OP cross sections in panels (a) and (c) while BPRM σ_{PI} [18] filled with resonant structures. These high-peak resonances in BPRM cross section indicate orders of magnitude higher probability of photoionization. Hence without inclusion of $n = 3$ core states, σ_{PI} is considerably underestimated and give lower opacity as concluded by the observed spectra of the Z-pinch experiment by Bailey et al. [1].

7.5.3 Monochromatic Opacities

Often it is expected that only the ground state and low-lying metastable states in a plasma are significantly populated. The ionization fractions and level populations are computed using an equation-of-state, such as the modified Boltzmann-Saha formulation in the ‘chemical picture’ [9], based on the assumption that isolated atoms exist, albeit perturbed by the plasma environment [27]. At low densities and temperatures the ion fractions and occupation probabilities of high-lying levels are several orders of magnitude smaller than those for the ground state and metastable levels. But in the high temperature-density regime $N_e > 10^{24} \text{ cm}^{-3}$, $T_e > 10^6 \text{ K}$, similar to

that in the solar convection zone, electron-ion recombination rates can be large, and increase rapidly as N_e^2 . Even a small population in excited levels would then be susceptible to the resonant enhancements due to PEC resonances, which are currently neglected and the cross sections for excited levels are taken to be nearly hydrogenic, instead of the accurate form exemplified in Figs. 7.3, 7.4 and 7.5.

Monochromatic opacity spectra are sampled at approximately 10,000 points (viz. [28, 29]), although the atomic data are much more finely resolved. It has been verified that the statistical averages of the most important quantity, the Rosseland Mean Opacity (RMO), do not deviate by more than 1–3 % even if the atomic cross sections are ‘sampled’ at 10^5 or 10^6 points [27] and the energy mesh of $\sim 30,000$ points predominantly in the region of covered by the high energy $n = 3$ resonances, should suffice.

Figure 7.6 presents the monochromatic opacity κ (Fe XVII) computed using all of the bound-free, that is, photoionization data of 454 bound levels resolved with fine energy mesh. The calculations are carried out using a newly developed code for high-precision opacities, adapted from the earlier OP work [27]. The new code also employs a frequency mesh of 10^5 points, an order of magnitude finer mesh than OP or OPAL, thus obviating some resolution issues in the monochromatic opacity spectra [31]. Other components of the opacity calculations related to bound-bound transitions are retained as in the OP code: electron-impact and Stark broadening, free-free scattering, and electron-photon interaction in the Rayleigh, Thomson, and Compton scattering limits. However, resonance profiles have not yet been broadened. Details of the computations are given in [20].

Since the resonances would dissolve more readily than lines, it is likely to significantly affect *continuum lowering*, manifest in opacity spectra, are highly sensitive to temperature and density. Lines dissolve and eventually merge into the continuum in high temperature-density regime. Then a precise accounting may not be necessary; they are often treated as “unresolved transition arrays” (UTA) since J-J’ transitions are merged together and often subsumed by line broadening [25]. However, our aim is to focus on delineation of atomic features as fully as possible so that their contributions to opacity in different temperature-density regimes can be accurately ascertained.

The BPRM opacity cross sections in Fig. 7.6 are compared to two other sets of results from OP. Although over 20,000 oscillator strengths for bound-bound transitions are also computed, we use the same data for lines as the earlier OP calculations [27]. Thus the differences between the 60CC BPRM results from the present work in the upper panel of Fig. 7.6, and the limited OP without resonances in the middle panel, are entirely due to the differences in the bound-free data sets. The opacity calculations are done at a temperature-density representative of the plasma conditions at the base of the solar convection zone: $\log_{10} T(\text{K}) = 6.35$ and $\log_{10} N_e = 23$. In addition to resonance contributions, there are some other differences. The OP data include extrapolated cross sections out to very high energies, ~ 500 Ry. The BPRM data have also been processed to include these high-energy “tails”, but the form is slightly different. The background opacity is important to obtain a value for RMOs that spans over 4 decades in temperature, $\log_{10} T(\text{K}) = 3.5\text{--}7.5$.

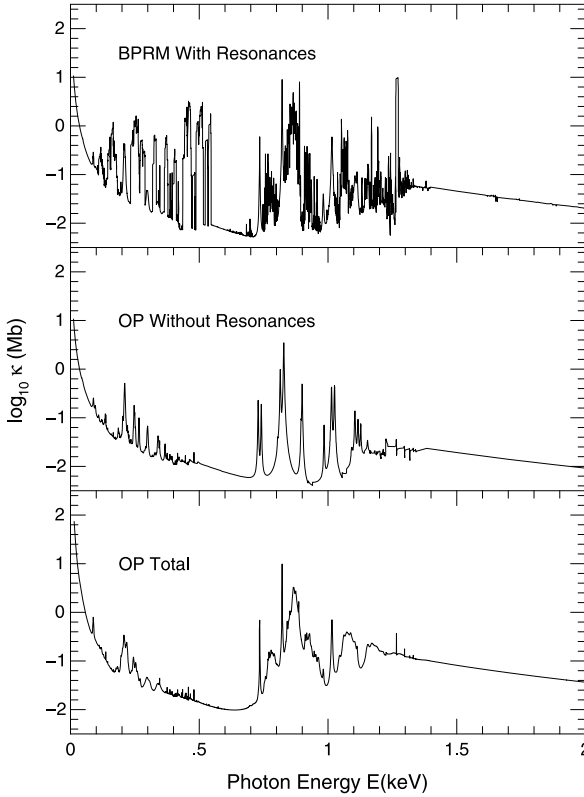


Fig. 7.6 Partial monochromatic opacity of Fe XVII: $\log_{10} \kappa$ (Mb) at temperature $T = 2.24 \times 10^6$ K and electron density $N_e = 10^{23} \text{ cm}^{-3}$, corresponding to the base of the solar convection zone where the Fe XVII ion is the largest contributor to opacity. *Top*: Opacities using BPRM photoionization cross sections with resonances computed with 60CC wave function; *Middle*: Without resonances using earlier data from the Opacity Project. Identical dataset for oscillator strengths from the OP is employed, that is, the differences are mainly due to the resonances in the 60CC calculations. *Bottom*: For comparison, total OP opacities [31] that include core-excitation resonances as lines, with autoionization widths considered perturbatively, as well as the high-energy K-shell continuum opacity not yet included in BPRM calculations

The BPRM value of κ_R , including the bound-bound oscillator strengths computed in this work (as opposed to OP) yields a value of $223.8 \text{ cm}^2/\text{g}$. Using the same bound-bound data as OP, the BPRM κ -value is still $200.3 \text{ cm}^2/\text{g}$, compared to the OP value of $109.7 \text{ cm}^2/\text{g}$ (Fig. 7.6). The bottom panel in Fig. 7.6 is the total monochromatic opacity spectrum of Fe XVII from OP, including all contributions, with the total RMO $\kappa_R = 306.9 \text{ cm}^2/\text{g}$. Thus the BPRM value using the data computed in this work is 27 % lower. This is primarily because of two factors missing in the BPRM calculations: (I) The high-energy “tails” including the K-ionization thresholds are missing. (II) The bound-bound oscillator strengths are computed up to $n = 10$. A relatively small gap in cross sections in the region between $n = 10$ – ∞ ,

below the photoionization thresholds of the 454 bound levels are also missing. Following OP work, the tabulation of cross sections at $E = -z^2/v^2$ ($v \sim 10$) below each threshold was carried out resulting in BPRM RMO value from 223.8 cm²/g to 260.7 cm²/g, to within 20 % of the total OP RMO. These differences are being investigated.

7.6 Conclusion

The comprehensive calculations were carried out so as to compare with the erst-while OP calculations that treated resonances as lines and effect of accuracy, correct features and completeness of atomic data on resolving the solar abundances and opacity in the convection zone. A clear distinction is made between pure bound-bound transitions and bound-free transitions into autoionizing levels. The results from this work demonstrate that opacities may be computed using BPRM cross sections and transition probabilities, and it is likely that plasma opacities in general, and those of Fe ions in particular, would be different from earlier ones using atomic cross sections that accurately consider the energy distribution of resonances.

Acknowledgements Partial supports from NSF and DOE are acknowledged. Computations were carried out at the Ohio Supercomputer Center.

References

1. J.E. Bailey et al., in *51st Annual Meeting of the Division of Plasma Physics (DPP) of APS*, Atlanta, Georgia, November 2–6 (2009) TOc.010 (22 authors)
2. K.A. Berrington et al., *J. Phys. B* **20**, 6379 (1987)
3. K.A. Berrington et al., *Comput. Phys. Commun.* **92**, 290 (1995)
4. W. Eissner, G. Chen (unpublished)
5. W. Eissner, M. Jones, H. Nussbaumer, *Comput. Phys. Commun.* **8**, 270 (1974)
6. D.G. Hummer et al., *Astron. Astrophys.* **279**, 298 (1993)
7. C.A. Iglesias, F.J. Rogers, *Astrophys. J.* **371**, 40 (1991)
8. C.A. Iglesias, F.J. Rogers, *Astrophys. J.* **464**, 943 (1996)
9. D. Mihalas, D.G. Hummer, W. Däppen, *Astrophys. J.* **331**, 815 (1988)
10. S.N. Nahar, *Astron. Astrophys. Suppl. Ser.* **127**, 253 (2000)
11. S.N. Nahar, *Astron. Astrophys.* **448**, 779 (2006)
12. S.N. Nahar, *Astron. Astrophys.* **457**, 721 (2006)
13. S.N. Nahar, *J. Quant. Spectrosc. Radiat. Transf.* **109**, 2417–2426 (2008)
14. S.N. Nahar, *At. Data Nucl. Data Tables* **97**, 403 (2011)
15. S.N. Nahar, A.K. Pradhan, *Phys. Scr.* **61**, 675 (2000)
16. S.N. Nahar, A.K. Pradhan, *Astron. Astrophys.* **437**, 345 (2005)
17. S.N. Nahar, A.K. Pradhan, H.L. Zhang, *Phys. Rev. A* **63**, 060701 (2001). *Rapid Commun.*
18. S.N. Nahar, W. Eissner, G.X. Chen, A.K. Pradhan, *Astron. Astrophys.* **408**, 789 (2003)
19. S.N. Nahar, M. Montenegro, W. Eissner, A.K. Pradhan, *Phys. Rev. A* **82**, 065401 (2010). *Brief Report*
20. S.N. Nahar, A.K. Pradhan, G.X. Chen, W. Eissner, *Phys. Rev. A* **83**, 053417 (2011)

21. NORAD-Atomic-Data, www.astronomy.ohio-state.edu/~nahar/nahar_radiativeatomicdata/index.html
22. OPSEver, <http://opacities.osc.edu>
23. A.K. Pradhan, S.N. Nahar, in *Atomic Astrophysics and Spectroscopy* (Cambridge University Press, Cambridge, 2011)
24. A.K. Pradhan, S.N. Nahar, H.L. Zhang, *Astrophys. J. Lett.* **549**, L265–L268 (2001)
25. B.F. Rozsnyai, S.D. Bloom, D.A. Resler, *Phys. Rev. A* **44**, 6791 (1991), and references therein
26. M.J. Seaton, *J. Phys. B* **20**, 6363 (1987)
27. M.J. Seaton, Y. Yu, D. Mihalas, A.K. Pradhan, *Mon. Not. R. Astron. Soc.* **266**, 805 (1994)
28. The Opacity Project Team, *The Opacity Project*, vol. 1 (IOP Publishing, Bristol, 1995)
29. The Opacity Project Team, *The Opacity Project*, vol. 2 (IOP Publishing, Bristol, 1996)
30. TIPbase, <http://cdsweb.u-strasbg.fr/tipbase/home.html>
31. TOPbase, <http://vizier.u-strasbg.fr/topbase/topbase.html>
32. Y. Yu, M.J. Seaton, *J. Phys. B* **20**, 6409 (1987)
33. H.L. Zhang, S.N. Nahar, A.K. Pradhan, *Phys. Rev. A* **64**, 032719 (2001)